single, spin-polarized electronic ground state, separated from all excited states by an energy gap Δ, with $\Delta \gg 0.1$ meV (the thermal energy kT at 1.2 K). Nuclear spin-lattice relaxation can occur only in the excited states, making $1/T_1$ small and temperature-dependent. For $2/3 < \nu < 1$, there is a manifold of low-energy electronic states, with energy width δ. These states have varying degrees of electron spin polarization, so that nuclear spin relaxation can take place rapidly within the low-energy manifold [and Δf is smaller than at $\nu = 1$, as observed (9)]. If $\delta < 0.1$ meV and $\Delta' \gg 0.1$ meV, $1/T_1$ will be nearly temperature-independent over the range of our measurements (*16*). At $\nu = 2/3$, there is again a single electronic ground state, separated from higher energy states by Δ''. If $\Delta'' \gtrsim 0.1$ meV, $1/T_1$ is again relatively small and temperature-dependent (*17*). The reduced spin polarization of the low-energy states for $2/3 < \nu < 1$ (and of the excited states), the energy gap Δ'', and the energy width δ are consequences of electron-electron interactions. This picture of the many particle states is generally consistent with transport measurements (*1*, *18*), which show $\Delta'' \approx$ 0.1 to 0.5 meV at $\nu = 2/3$ and 9.39 T, and calculations (*19*), which suggest that the spin polarization of the low-energy states at $\nu = 1 \pm \varepsilon$ is strongly reduced by electron-electron interactions. Our results show that, in a real 2DES, there exist nearly degenerate electronic states with different values of $\langle S_{z'} \rangle$ and suggest that the energy gaps for electronic spin excitations at $\nu = 2/3$ and $\nu = 1$ are similar to the energy gaps for charge excitations.

A more quantitative understanding of the energy splittings and spin polarizations is to be expected from additional OPNMR measurements. Although samples with multiple quantum wells were used in the experiments reported here, the OPNMR signals from the wells are sufficiently strong and resolved from barrier and substrate signals that similar measurements on single quantum wells ($\lesssim 10^{16}$ ^{71}Ga nuclei) should be possible.

REFERENCES AND NOTES

1. J. T. Devreese and F. M. Peeters, *The Physics of the Two-Dimensional Electron Gas* (Plenum, New York, 1987); J. P. Eisenstein and H. L. Stormer, *Science* **248**, 1510 (1990); J. K. Jain, *ibid.* **266**, 1199 (1994).
2. C. Weisbuch and B. Vinter, *Quantum Semiconductor Structures* (Academic Press, San Diego, 1991), pp. 123–139.
3. S. E. Barrett, R. Tycko, L. N. Pfeiffer, K. W. West, *Phys. Rev. Lett.* **72**, 1368 (1994).
4. G. Lampel, *ibid.* **20**, 491 (1968); D. Paget, G. Lampel, B. Sapoval, V. I. Safarov, *Phys. Rev. B* **15**, 5780 (1977); G. P. Flinn, R. T. Harley, M. J. Snelling, A. C. Tropper, T. M. Kerr, *Semicond. Sci. Technol.* **5**, 533 (1990); V. K. Kalevich, V. L. Korenev, O. M. Fedorova, *JETP Lett.* **52**, 349 (1990); M. Krapf, G. Denninger, H. Pascher, G. Weimann, W. Schlapp, *Solid State Commun.* **78**, 459 (1991); S. K. Buratto, D. N. Shykind, D. P. Weitekamp, *Phys. Rev. B* **44**, 9035 (1991); *J. Vac. Sci. Technol. B* **10**, 1740 (1992).
5. For recent examples, see: R. Tycko, *J. Phys. Chem. Solids* **54**, 1713 (1993); R. Tycko *et al.*, *Science* **253**, 884 (1991); R. E. Walstedt and W. W. Warren Jr., *ibid.* **248**, 1082 (1990); J. A. Martindale *et al.*, *Phys. Rev. Lett.* **68**, 702 (1992).
6. D. Suter and R. R. Ernst, *Phys. Rev. B* **32**, 5608 (1985); R. Tycko and G. Dabbagh, *Isr. J. Chem.* **32**, 179 (1992).
7. J. Winter, *Magnetic Resonance in Metals* (Oxford Univ. Press, London, 1971).
8. S. L. Richardson, M. L. Cohen, S. G. Louie, J. R. Chelikowsky, *Phys. Rev. B* **33**, 1177 (1986).
9. S. E. Barrett, G. Dabbagh, L. N. Pfeiffer, K. W. West, R. Tycko, *Phys. Rev. Lett.*, in press.
10. Numerical simulations of the dependence of the OPNMR spectra on τ_D, based on the equation

$$\frac{\partial p}{\partial t} = D\frac{\partial^2 p}{\partial z^2} - \frac{1}{T_1(z)}(p - p_{\mathrm{eq}})$$

for the nuclear spin polarization $p(z,t)$ with $T_1(z) \propto \rho(z)^{-2}$, indicate that the effective diffusion constant D for nuclear spin diffusion between wells and barriers is less than 10 Å^2 s^{-1} for all ν under our experimental conditions. Spin diffusion reduces the apparent T_1 for well nuclei by less than 10%.
11. A. Berg, M. Dobers, R. R. Gerhardts, K. v. Klitzing, *Phys. Rev. Lett.* **64**, 2563 (1990).
12. S. V. Iordanskii, S. V. Meshkov, I. D. Vagner, *Phys. Rev. B* **44**, 6554 (1991).
13. D. Antoniou and A. H. MacDonald, *ibid.* **43**, 11686 (1991).
14. Y. N. Ovchinnikov, I. D. Vagner, A. M. Dyugaev, *JETP Lett.* **59**, 569 (1994).
15. J. H. Kim, I. D. Vagner, L. Xing, *Phys. Rev. B* **49**, 16777 (1994).
16. In principle, particular combinations of the many-particle density of states and the matrix elements $\langle \mathrm{f}, p\pm 1 | H_h | \mathrm{i}, p \rangle$ could give rise to a temperature-independent $1/T_1$ without requiring an energy gap. This seems an unlikely possibility.
17. An excitation energy gap is also expected at $\nu = 4/3$. The corresponding minimum in $1/T_1$ is not apparent in Fig. 4 either because the data points are too widely spaced or because the gap is significantly smaller than that at $\nu = 2/3$.
18. G. S. Boebinger, A. M. Chang, H. L. Stormer, D. C. Tsui, *Phys. Rev. Lett.* **55**, 1606 (1985); J. E. Furneaux, D. A. Syphers, A. G. Swanson, *ibid.* **63**, 1098 (1989).
19. S. L. Sondhi, A. Karlhede, S. A. Kivelson, E. H. Rezayi, *Phys. Rev. B* **47**, 16419 (1993); H. A. Fertig, L. Brey, R. Côté, A. H. MacDonald, *ibid.* **50**, 11018 (1994).

18 January 1995; accepted 20 March 1995

Monodisperse Metal Clusters 10 Angstroms in Diameter in a Polymeric Host: The "Monomer as Solvent" Approach

Josh H. Golden, Haibin Deng, Francis J. DiSalvo,
Jean M. J. Fréchet,* Patrick M. Thompson

A general methodology is presented for the dispersion of an inorganic compound within an organic polymer host through the use of solubilizing and polymerizable ligands. The dispersion of metal cluster cations 10 angstroms in diameter within a polymer host is achieved by free-radical polymerization of the hexafunctional metal cluster [$\mathrm{Mo_6Cl_8(NVI)_6}$](triflate)$_4$ with bound polymerizable ligands in *N*-vinylimidazole (NVI) solutions. Copolymerization of the activated cluster-bound ligands with the surrounding medium probably plays a key role in preventing aggregation and produces near monodisperse molecular clusters within the polymer matrix.

Intense research efforts are now being focused on the design and fabrication of materials that contain metal nanoclusters (1 to 10 nm) because of real and potential applications of these materials in optics and electronics (*1*). Nanoscale metal clusters display a variety of useful physical properties including catalysis (*1*, *2*), magnetism (*3*), and size-dependent light absorption (the quantum size effect) (*1*, *4*, *5*). A major challenge in the preparation of these materials is the prevention of both phase separation and aggregation of the clusters within the host matrix. Strategies used to control cluster aggregation, size, and morphology include the electrochemical synthesis of surfactant-stabilized clusters (*1*), in situ formation of metal clusters in the polar segments of diblock copolymers (*5*), and metal vapor deposition (*1*, *6*). We now report a general methodology for the preparation of near monodisperse nanoclusters in a polymer host by cluster copolymerization with a solubilizing monomer-solvent medium.

Our strategy, termed the "monomer as solvent" approach, involves the design of a monomer that can act as both a ligand and a solvent for the metal nanoclusters. In this approach, phase separation is not expected because the vinyl-functionalized clusters are an integral part of the polymerization system. In effect, they act as the loci for cross-linking of the surrounding dispersing medium. To achieve this goal, it is first necessary to identify a polar organic solvent that also acts as a ligand. Structurally related mono-

---

J. H. Golden, H. Deng, F. J. DiSalvo, J. M. J. Fréchet, Department of Chemistry, Baker Laboratory, Cornell University, Ithaca, NY 14853, USA.
P. M. Thompson, Eastman Kodak Company, Rochester, NY 14650, USA.

*To whom correspondence should be addressed.

mers that retain the solubilizing characteristics of the nonpolymerizable solvent are then examined. Some possible solvent and monomer combinations are illustrated in Fig. 1. Finally, the inorganic compound is dissolved in the monomer in which ligand exchange occurs. The resulting homogeneous solution is then subjected to free-radical polymerization that is initiated either thermally or photochemically.

This design allows the dispersion scale to be tuned by adjustment of the concentration of the dissolved clusters in the monomer solution. The kinetics of polymerization must be fast in order to ensure that the gel point is reached early, so that phase separation or aggregation processes do not occur. Because the polymerizable ligands are bound to the cluster surface, the goals of fast solidification and chemical association of the metal clusters with the supporting matrix are achieved simultaneously.

The family of metal clusters we chose for dispersion is $[Mo_6Cl_8(L)_6]^n$, where $n = 4+$ when L is a neutral ligand, or $n = 2-$ when L is a monovalent anion. The photoredox and luminescent behaviors of these clusters may be tuned by varying the identity of L, and they are chemically stable in corrosive media (*7*). The structure of $[Mo_6Cl_8(L)_6]^n$ is represented in Fig. 2 (*8*, *9*). We have used the metathetic substitution chemistry developed by Johnston, Shriver, and co-workers (*9*) to prepare the metal cluster with bound monomer ligands. The six *N*-vinylimidazole (NVI) ligands are bound to axial positions of the cluster by replacement of weakly bound triflate (OTf) ligands (scheme 1; Bu, butyl; ppt, precipitate); an excess of NVI is used during the preparation to ensure complete substitution.

$$(NBu_4)_2[Mo_6Cl_8(OTf)_6] + 12\ NVI \xrightarrow[CH_2Cl_2]{23°C} [Mo_6Cl_8(NVI)_6](OTf)_{4\ (ppt)} + 2NBu_4OTf + 6\ NVI$$

Analyses of the yellow polycrystalline $[Mo_6Cl_8(NVI)_6](OTf)_4$ by ^1H nuclear magnetic resonance (^1H NMR), ultraviolet-visible (UV-vis), and infrared (IR) spectroscopy confirmed that the NVI ligands are bound to the octahedral Mo framework. The ^1H NMR signals of the six NVI protons are shifted downfield significantly as compared to unbound NVI (*10*). The polarization of the electron density from the NVI ligands toward the 4+ charged cluster is also observed in the UV-vis spectrum of the cluster. The π to π^* transitions for the bound NVI ligands (190 and 204 nm) are shifted to higher energies as compared to unbound NVI (196 and 238 nm). This shift is due to the lower energy of the bound NVI highest occupied molecular orbital, resulting in a greater gap between the highest occupied molecular orbital and the lowest unoccupied molecular orbital. The broad ligand-to-metal charge-transfer band characteristic of this class of metal clusters is also observed at 350 nm (*9*). The IR spectrum displays absorptions that are attributed to unbound OTf species, as well as bound NVI ligands (*11*), and the elemental analysis is consistent with the assigned stoichiometry (*12*).

The cluster-polymer dispersion was prepared by bulk polymerization of the light yellow solutions of $[Mo_6Cl_8(NVI)_6](OTf)_4$ clusters in the NVI monomer-solvent. After addition of 1 mol % of 2,2′-azobis(isobutyronitrile), the free-radical initiator, the transparent homogeneous 0.10 and 0.50 M cluster-monomer solutions contained in argon-purged sealed ampoules were cured by immersion in an oil bath equilibrated at 70°C for 24 hours. Complete solidification was observed within 15 to 20 min, with some darkening to yellow-amber. Despite this slight darkening, no new absorptions were observed in the visible spectrum of the polymerized solid. In contrast, polymerization of neat NVI under identical conditions produced no color change or darkening, and solidification only appeared complete after

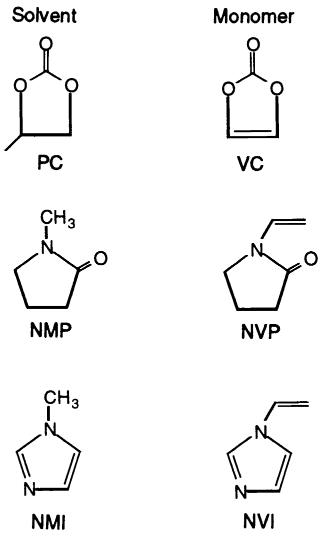

Fig. 1. Polar solvents and their respective monomer counterparts with similar solubility properties: propylene carbonate (PC) and vinylene carbonate (VC); *N*-methylpyrrolidone (NMP) and *N*-vinylpyrrolidone (NVP); *N*-methylimidazole (NMI) and *N*-vinylimidazole (NVI).

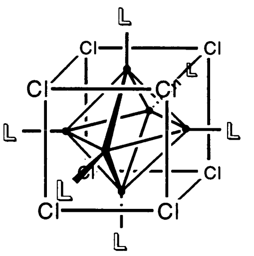

Fig. 2. The $[Mo_6Cl_8(L)_6]^n$ (n = 4+ or 2−) cluster consists of an octahedral framework of Mo atoms, substitutionally inert face-capping Cl atoms, and six axial ligands L, that may be neutral or may have a charge of 1−.

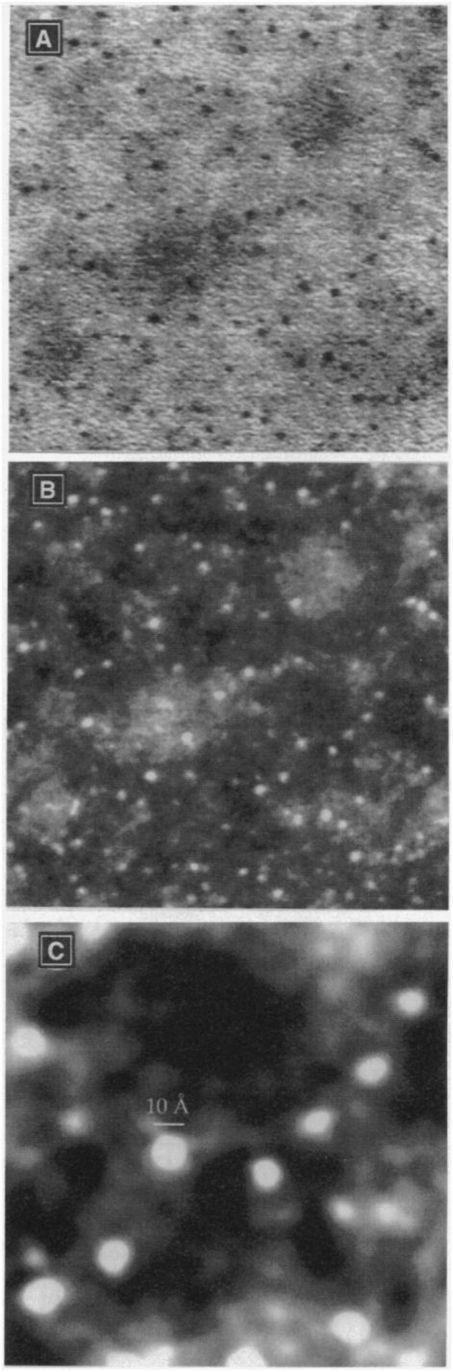

Fig. 3. (**A**) Phase-contrast bright-field image and (**B**) *Z*-contrast dark-field image of 0.50×10^{-3} M cluster material at 10^6 magnification. The average features are ~10 Å in diameter, which corresponds to the ionic radius of a single $[Mo_6Cl_8]^{4+}$ cluster. The horizontal field of view for both images is 10^3 Å. (**C**) A constellation of clusters ~10 Å in diameter at 7.8×10^6 magnification. The horizontal field of view is 128 Å.

2.5 to 3 hours. The 10-fold decrease in time to solidification is the result of the cross-linking derived from the incorporation of the hexavinyl clusters into the polymerization mixture.

The extent of swelling of a polymer is generally inversely proportional to its degree of cross-linking. Poly(NVI) prepared under identical conditions is soluble in dimethyl sulfoxide (DMSO). In contrast, the opaque 0.10 M cluster-polymer dispersion swelled to twice its size after 24 hours at 23°C. After 1 month of equilibration, the UV-vis spectrum of the yellow DMSO extract displayed a broad absorption at ~270 nm, characteristic of the cluster-DMSO adduct (*13*). This result suggests that DMSO is a stronger binding ligand than NVI and is thus able to extract some of the clusters from within their polymer matrix.

The highly cross-linked, transparent 0.50 M cluster-polymer displayed little or no swelling in deuterated DMSO (DMSO-d_6), even after 6 months at 23°C. If we assume cluster–bound NVI copolymerization and six cross-linking sites per cluster, an increase in $[Mo_6Cl_8(NVI)_6](OTf)_4$ concentration from 0.10 to 0.50 M provides a 30-fold increase in cross-linking sites, resulting in a material with a very high cross-link density. The glass transition temperature (T_g) data are consistent with this expected increase in cross-link density as T_g values increased from 164°C for neat poly(NVI) to 220°C for the 0.10 M cluster-polymer and 257°C for the 0.50 M material.

Time-of-flight secondary-ion mass spectrometry (TOF-SIMS) is a useful technique for probing the surface (≤ 20 Å) composition of polymers and composites as well as metal clusters (*14*, *15*). Because the 0.50 M cluster-polymer is insoluble, we used TOF-SIMS to probe the interaction of the clusters with the poly(NVI) host. The positive ion TOF-SIMS spectrum of $[Mo_6Cl_8(NVI)_6](OTf)_4$ displayed the expected isotopic array of peaks for intact $[Mo_6Cl_8(NVI)_x]^{4+}$ ($x = 0, 1, 2$) clusters at 860, 954, and 1048 atomic mass units (amu), in addition to peaks corresponding to $(Mo_5Cl_6)^{4+}$, $(Mo_4Cl_4)^{4+}$, and the array of Mo^+ isotopes centered at 96 amu. In contrast, intact $[Mo_6Cl_8(NVI)_x]^{4+}$ ($0 \leq x \leq 6$) clusters could not be observed in the positive ion spectrum of the 0.50 M cluster-polymer, reflecting the low probability of desorption of an intact, multiply bound cluster from the polymer matrix. The bound clusters at the surface of the 0.50 M material were decomposed by the Ga^+ beam of the spectrometer, as revealed by the positive-ion spectrum, which displayed the array of elemental Mo isotope peaks, albeit at significantly lower intensity than that observed for the neat cluster spectrum. The negative ion spectrum of the cluster-polymer displayed a variety of low-mass species, including Cl^- and OTf.

We probed the nanoscale homogeneity of the 0.50 M cluster-polymer, from 200 to 50 nm, by quantitative scanning electron microscopy (SEM) and x-ray powder diffraction. The SEM microprobe analysis, conducted in terms of Mo Kα ratios, confirmed the elemental homogeneity of the concentrated 0.50 M material. Random areas of the sample scanned with electron beam diameters from 20 μm to 200 nm (respective volumes of 300 μm^3 and 3×10^4 nm^3) yielded a Mo content of 13 to 15% (by weight) versus a theoretical value of 13.6%.

The x-ray powder diffraction pattern of $[Mo_6Cl_8(NVI)_6](OTf)_4$ revealed the crystalline nature of the cluster-monomer adduct. The highest intensity peak at $\sim 2\theta = 6.5°$ (θ is the dispersion angle; the interatomic d spacing is 14.75 Å) is consistent with the large unit cell parameters reported for similar cluster compounds (*8*, *9*). In contrast to the case for crystalline $[Mo_6Cl_8(NVI)_6](OTf)_4$, the x-ray powder diffraction pattern of the 0.50 M cluster-polymer material revealed nothing beyond noise level in a typical scan from $2\theta = 5°$ to 80°. The fact that no sharp diffraction peaks were observed indicates that no crystalline cluster aggregation (>50 nm particle size) within the polymer host had occurred.

We carried out angstrom scale analysis through scanning transmission electron microscopy (STEM) and energy-dispersive x-ray absorption (EDAX) (*16*). Samples for these analyses were prepared by polymerization of the cluster solutions on C-coated Cu grids under Ar. Phase-contrast (bright-field) and Z-contrast (dark-field) (Z is atomic number) images of the 0.50 M cluster-polymer at 10^6 magnification did not display discrete metal clusters or aggregates and showed only the mottled appearance that is typical of an amorphous polymer. This finding suggests that, even at relatively high concentrations, the Mo clusters are near monodisperse and do not phase-separate. However, at this concentration, "overlap" of the ~75,000 clusters in the beam volume of 1000 Å by 1000 Å by 250 Å prevents observation of an individual cluster cation 10 Å in diameter (*17*).

To image an individual cluster, we found it necessary to dilute the clusters in the polymer by a factor of 1000. A dilution to 0.50×10^{-3} M corresponds to only ~75 clusters per image volume; as a result of this dilution, the clusters are less likely to overlap in the beam volume. The STEM images of the 0.50×10^{-3} M cluster-polymer (Fig. 3, A and B) show a population of cluster sizes ranging from 10 to 30 Å in both phase-contrast and Z-contrast modes. Because of the depth of focus of the imaging technique (~400 Å), the small range of sizes may be a result of some cluster overlap in the field of view or of cluster copolymerization. Figure 3C shows a "constellation" of monodisperse clusters ~10 Å in diameter. EDAX analysis of the individual clusters and bulk areas (10^4 $Å^2$) yielded weight percent values consistent with intact $[Mo_6Cl_8]^n$ clusters (*18*). In EDAX mode, decomposition of the individual clusters in the stationary beam (~10 Å beam diameter) was observed in 2 to 5 s; therefore, we found it necessary to sample at least 10 clusters to obtain statistically significant data.

The homogeneity of the cluster dispersion is generally very good in most random sample areas where the clusters are easily imaged by STEM. Although Fig. 3B shows an average of 120 ± 11 clusters versus the estimated value of ~75 clusters per image volume, this difference can easily vary as a result of small variations in estimated sample thickness and small variations in the procedure used to prepare the very dilute cluster-polymer STEM samples.

This study demonstrates the versatility of the "monomer as solvent" approach for the preparation of molecular dispersions of metal nanoclusters in organic polymer hosts. The reactive functionalization of the metal cluster surface with bound polymerizable ligands provides a pathway that allows the clusters to chemically bind with the host matrix. The fast polymerization and cross-linking of the activated cluster-bound monomers with the surrounding medium enhances the dispersion of the inorganic material within the polymer, even at high concentrations.

REFERENCES AND NOTES

1. M. T. Reetz *et al.*, *Science* **267**, 367 (1995), and references therein.
2. L. N. Lewis, *Chem. Rev.* **93**, 2693 (1993).
3. A. M. T. Nguyen and A. F. Diaz, *Adv. Mater.* **11**, 858 (1994); R. F. Ziolo *et al.*, *Science* **257**, 219 (1992).
4. A. Hagfelt and M. Grätzel, *Chem. Rev.* **95**, 49 (1995); Y. Yuan, J. H. Fendler, I. Cabasso, *Chem. Mater.* **4**, 312 (1992); M. E. Wozniak, A. Sen, A. L. Rheingold, *ibid.*, p. 753.
5. V. Sankaran, J. Yue, R. E. Cohen, R. R. Schrock, R. J. Silbey, *Chem. Mater.* **5**, 1133 (1993).
6. C. G. Francis, H. Huber, G. A. Ozin, *Inorg. Chem.* **19**, 219 (1980).
7. A. W. Maverick and H. B. Gray, *J. Am. Chem. Soc.* **103**, 1298 (1981); A. W. Maverick, J. S. Najdzionek, D. MacKenzie, D. G. Nocera, H. B. Gray, *ibid.* **105**, 1878 (1983); R. D. Mussell and D. G. Nocera, *Inorg. Chem.* **29**, 3711 (1990).
8. C. Brosset, *Ark. Kemi, Mineral. Geol. A* **20** (no. 7), 1 (1945); W. Preetz, K. Harder, H. G. von Schnering, G. Kliche, K. Peters, *J. Alloys Compd.* **183**, 413 (1992).
9. D. H. Johnston, D. C. Gaswick, M. C. Lonergan, C. L. Stern, D. F. Shriver, *Inorg. Chem.* **31**, 1869 (1992).
10. ^1H NMR data: NVI (200 MHz, CD_3NO_2): chemical shift δ 4.89 [d, 1H, vinyl H(*trans*)], δ 5.37 [d, 1H, vinyl H(*cis*)], δ 7.06 [m, 1H, vinyl H(gem)], δ 7.00, 7.34, and 7.69 (s, 3H, ring). Bound NVI (200 MHz, CD_3NO_2): δ 5.33 [d, 1H, vinyl H(*trans*)], δ 5.75 [d, 1H, vinyl H(*cis*)], δ 7.27 [m, 1H, vinyl H(gem)], and δ 7.51, 7.81, and 8.68 (s, 3H, ring).
11. The IR spectrum exhibited a (C–H) azole absorption

at 3126 cm^{-1}, aromatic ring modes at 1518 cm^{-1}, and the vinyl (C=C) stretch at 1650 cm^{-1}. Unbound OTf absorptions were observed at ~1032, 1165, and 1280 cm^{-1}.

12. Elemental analysis (percent by weight) calculated for $C_{34}H_{36}Cl_8F_{12}Mo_6N_{12}O_{12}S_4$: C, 20.21; H, 1.80; N, 8.32. Found: C, 20.24; H, 1.55; N, 8.30.
13. F. A. Cotton and N. F. Curtis, *Inorg. Chem.* **4**, 241 (1965).
14. A. R. Waugh, D. R. Kingman, M. J. Hearn, D. Briggs, in *Secondary Ion Mass Spectrometry, SIMS 4*, A. Benninghoven, A. M. Huber, H. W. Werner, Eds. (Wiley, New York, 1988), pp. 231–234.
15. H. A. Hodali, H. Hung, D. F. Shriver, *Inorg. Chim. Acta* **198–200**, 245 (1992).
16. The STEM images were obtained with a Vacuum Generators HB-501A STEM equipped with an analytical pole piece (coefficient of spherical aberration C_s = 3.3 mm) at 100 keV. The theoretical resolution limit is 2.7 Å, and the pressure in a working vacuum was ~10^{-10} torr. EDAX was performed with a Link AN10000 system with a liquid nitrogen–cooled windowless Si(Li) detector. We calculated weight percent values for Mo and Cl using Cliff-Lorimer quantitative x-ray compositional analysis by Thin Film Analysis 1.3, a public domain software; *K* factors were calculated.
17. The approximate diameter of a $[Mo_6Cl_8]^{4+}$ cluster was estimated by calculation of the cubic body diagonal length (Cl–Cl = 6 Å) and the addition of two Cl^- ionic radii (Cl^- = 1.8 Å).
18. Individual clusters: theoretical percent by weight: Mo = 67, Cl = 33; EDAX percent by weight: Mo = 68 ± 8, Cl = 32 ± 2.

19. This work is dedicated to the memory of H. Deng. This work was supported by the MRL Materials Research Laboratory program of the National Science Foundation under award DMR-9121654. We thank J. Hunt, M. Thomas, and J. Silcox for aid in SEM, STEM, and EDAX analyses.

30 January 1995; accepted 10 April 1995

Ordered Metal Nanohole Arrays Made by a Two-Step Replication of Honeycomb Structures of Anodic Alumina

Hideki Masuda* and Kenji Fukuda

A highly ordered metal nanohole array (platinum and gold) was fabricated by a two-step replication of the honeycomb structure of anodic porous alumina. Preparation of the negative porous structure of porous alumina followed by the formation of the positive structure with metal resulted in a honeycomb metallic structure. The metal hole array of the film has a uniform, closely packed honeycomb structure approximately 70 nanometers in diameter and from 1 to 3 micrometers thick. Because of its textured surface, the metal hole array of gold showed a notable color change compared with bulk gold.

In recent years, there has been increasing interest in the fabrication of nanometer-sized fine structures because of their potential utilization in electronic, optical, and micromechanical devices. One approach to the fabrication of nanometer-sized structures has been to use a naturally occurring structure as a host for the fabrication (*1–6*). This approach is promising, especially for the preparation of large-area, nanometer-sized structures with high aspect ratios, which are difficult to form by a conventional lithographic process. Anodic porous alumina, which is prepared by the anodic oxidation of aluminum in an acidic electrolyte, is one of the typical self-organized fine structures with a nanohole array (*7*, *8*). Anodic porous alumina has a packed array of columnar hexagonal cells with central, cylindrical, uniformly sized holes ranging from 4 to 200 nm in diameter. Many types of nanocomposites have been fabricated with anodic porous alumina used as a host material; when used for the preparation of magnetic recording media (*9*, *10*), optical devices (*11*), functional electrodes (*12*, *13*), and electrochromic (*14*) and electroluminescence display devices (*15*), the holes in these materials are filled with metals or semiconductors.

We have developed a process for fabricating a nanohole array in which the honeycomb structure of anodic porous alumina is replaced through a two-step molding process (*16*). In this process, fabrication of the negative type of anodic porous alumina and subsequent formation of the positive type structure led to the formation of a porous metal and semiconductor with a geometrical structure identical to that of anodic porous alumina. An important aspect that distinguishes our two-step method from the conventional one-step embedding method is that it permits the full replication of the hole array of anodic porous alumina with desired materials. In this way, it is possible to overcome the disadvantages of using porous alumina, which include insufficient chemical and thermal stability and low mechanical strength.

In our early work (*16*), the regularity of the nanohole array in the replicated structure was unsatisfactory; this resulted from imperfections in the cell arrangement in the mother anodic porous alumina used as a starting material. In recent studies, we have found that notable regularity of the cell arrangement can be accomplished under appropriate anodizing conditions. In this report, we show the fabrication of an almost ideally arranged nanohole array of metals based on the ordered porous structure of anodic alumina and describe the change in color of the metal that occurs in the nanometer-sized honeycomb structure as compared to the bulk.

An outline of the typical fabrication process is presented in Fig. 1. High-purity aluminum (99.99%) was anodized in a 0.3 M oxalic acid solution under a constant voltage of 40 V. The cell arrangement of anodic porous alumina is usually far different from the ideally packed hexagonal columnar array. We have found that anodization under appropriate conditions can produce porous alumina with a highly ordered cell configuration. This process is characterized by a longer anodization period than would normally be necessary for the preparation of porous alumina by the application of a constant appropriate anodizing voltage.

Long period anodization at 40 V improved the regularity of the cell arrangement and produced an almost ideally arranged honeycomb structure. The defect-free regions appear in large domains, whereas defects can be found at the boundaries of these domains. The size of the domains was dependent on the anodization time. That is, the size of the defect-free region increased with the anodization time. The long period anodization rearranged the cells and reduced the number of defects and dislocations. After the anodization, we obtained the starting anodic porous alumina with through holes by removing the aluminum substrate and the bottom part of the porous layer with saturated $HgCl_2$. The specimen was then dipped into a 5% (by weight) phosphoric acid solution at 30°C to adjust the pore diameter.

The two-step replication was similar to that described in (*16*). A thin metal layer (5 nm thick) was deposited on the bottom side of anodic porous alumina by vacuum deposition. Usually the same metal as that intended for use as the porous material was used for the evaporation. This thin metal layer can act as a catalyst or electrode for the subsequent metal-plating process. Methyl methacrylate monomer containing 5% (by weight) benzoyl peroxide, which acted as an initiator for polymerization, was injected into the holes under vacuum conditions and was polymerized by ultraviolet irradiation. After removal of the alumina layer with 10% (by weight) NaOH, a replicated negative type of poly(methyl methacrylate) (PMMA) with a cylindrical structure was obtained. At the bottom part of the array of PMMA cyl-

---

Department of Industrial Chemistry, Faculty of Technology, Tokyo Metropolitan University, 1-1 Minamiosawa, Hachioji, Tokyo 192-03, Japan.

*To whom correspondence should be addressed.